Journal of Materials Processing Tech. 302 (2022) 117472

Contents lists available at ScienceDirect

Journal of Materials Processing Tech.

journal homepage: www.elsevier.com/locate/jmatprotec

Towards a generic physics-based machine learning model for geometry invariant thermal history prediction in additive manufacturing

Kari Lovise Ness [a,*], Arindam Paul [b], Li Sun [a], Zhiliang Zhang [a,*]

[a] Department of Structural Engineering, Norwegian University of Science and Technology (NTNU), Norway
[b] Independent Researcher, USA

ARTICLE INFO

Associate Editor: Robert Gao

Keywords:
Additive manufacturing
Machine learning
Feature engineering
Finite element method
Data-driven
Thermal predictions

ABSTRACT

Additive manufacturing (AM) is an emerging manufacturing technology that constructs complex parts through layer-by-layer deposition. The prediction and control of thermal fields during production of AM parts are of crucial importance as the temperature distribution and gradient dictates the microstructures, properties, and performance. Finite element (FE) analyses are commonly conducted to simulate the thermal history of the AM process, but are known to be costly and time-consuming. This paper aims to address the challenge by presenting the essential components of a generic data-driven control framework. The proposed framework utilizes extremely randomized trees and is trained and tested on datasets generated through FE simulations. The datasets contain generic, engineered features constructed based on the physics of the underlying thermal process. The features are transferable between a wide range of cases and have achieved mean absolute percentage errors (MAPE) below 2.5% for predicting nodal temperature profiles. In addition, predictions of entire simulations with machine learning (ML) models trained on datasets from different cases have been conducted with MAPE below 5%. The results demonstrate the transferability of thermal histories between several geometries and significantly reduce the need for expensive FE simulations. We believe that these findings are an important step towards real-time optimization in AM.

1. Introduction

Additive manufacturing (AM) is an emerging technology used for the industrial manufacturing of 3D parts (Watson and Taminger, 2018). As of today, AM is utilized across many industries, especially in cases where the manufacturing of intricate designs, low-volume, or one-of-a-kind manufacturing is important (Paul et al., 2019).

AM parts are built by iterative addition of thin layers of material according to a computer model (Groover, 2016). The process of constructing AM parts involves melting material by a focused energy source, followed by rapid consolidation (DebRoy et al., 2018). The steep thermal gradients and non-uniform expansion and contraction of the material during the thermal cycle may significantly impact the printed part performance by decreasing fatigue life, corrosion resistance, and increasing crack propagation, porosity, and geometrical distortions (Sun et al., 2021; Chew et al., 2015; Oliveira et al., 2020).

As physical experiments are expensive, computational simulations are essential in the design and optimization process to build robust and reliable parts (Adinarayanappa et al., 2017). However, due to complex boundary conditions and incremental element activation associated with the gradual deposition of material, modeling of the AM process has a high computational cost in processing time, memory, and computational requirements (Jiang et al., 2020). Recently, researchers have been interested in integrating finite element (FE) simulations and machine learning (ML) for real-time prediction of the AM process (Paul et al., 2019; Roy and Wodo, 2021; Ren et al., 2020; Zhou et al., 2021), where ML models predict the behavior of the expensive numerical methods. Due to the high level of redundancy, repeatability, and periodicity in the AM process, the process is well suited for ML. Machine learning implemented in AM is currently developed as a less expensive alternative to physics-based numerical models, where ML may accelerate the design and development in AM by enabling fast screening of parts. Several studies (Paul et al., 2019; Mozaffar et al., 2018; Roy and Wodo, 2021, 2020; Ren et al., 2020; Zhou et al., 2021) have proposed efficient, high-performance ML models and the fundamental framework for prediction of thermal fields in AM has already been established in previous works. However, due to numerous simplifications, the current ML models proposed by the scientific community deviate from the realistic responses when product properties such as geometry and deposition

* Corresponding authors.
E-mail addresses: karilov@icloud.com (K.L. Ness), zhiliang.zhang@ntnu.no (Z. Zhang).

https://doi.org/10.1016/j.jmatprotec.2021.117472
Received 29 August 2021; Received in revised form 14 December 2021; Accepted 19 December 2021
Available online 30 December 2021

Nomenclature

AM	additive manufacturing
ANN	artificial neural network
3D	3-dimensional
FDM	fused deposition modeling
FEA	finite element analysis
FFNN	feed-forward neural networks
ERT	extra tree
LBAM	laser-based additive manufacturing
MAE	mean absolute error
MAPE	mean absolute percentage error
RMSE	root mean squared error
α	thermal diffusivity
A	bead area
a	pass width
a_f	front semi-axes of double-ellipsoid heat source model
a_r	rear semi-axes of double-ellipsoid heat source model
d_e	Euclidean distance
f_f	fraction of deposited heat in front quadrant of double-ellipsoid heat source model
f_r	fraction of deposited heat in rear quadrant of double-ellipsoid heat source model
h_b	height of printing base
Q	power input
r	radius
r_P	Pearson correlation coefficient
r_S	Spearman correlation coefficient
ρ	density
T_{am}	ambient temperature
v	print speed
y_i	true value
$\widehat{y}_i$	predicted value

pattern becomes moderately complex (Mozaffar et al., 2021).

The work proposed in this paper addresses this problem by developing a generic feature set that captures the thermal processes without relying on simplifications of the parts. The proposed feature set is physics-based which can generalize across different geometries, deposition patterns, and power intensities and are extracted based on the underlying thermal processes in AM. The features are trained and tested on datasets that have been generated through numerical simulations of the thermal processes in additive manufacturing. These datasets have been generated to reflect various process characteristics such as deposition patterns, heat input, and geometry. The proposed approach presents several ML models that have been trained and tested on different datasets to ensure generalizability of the ML models when trained on various part characteristics. The ML models have demonstrated promising results in both same-simulation and simulation-to-simulation predictions. Same-simulation refers to the scenario where the ML model is trained and tested on data from the same simulation. On the other hand, simulation-to-simulation predictions are trained and tested on data from distinct sets of simulations. In particular, the capability to perform simulation-to-simulation predictions will reduce the time and computational cost compared to traditional numerical methods. Thus, we believe this work can bring the AM community closer to realizing the development of a comprehensive data-driven real-time control system for thermal predictions of AM processes.

The code used in this paper is published open-source at the following link: https://github.com/kariln/Predictions-of-thermal-fields-in-additive-manufacturing.

2. State-of-the-art of machine learning models for thermal predictions in additive manufacturing

The existing ML models for thermal prediction in AM are summarized in Table 1. Mozaffar et al. (2018) proposed a data-driven approach to predict the thermal behavior in a directed energy deposition (DED) process using time series in recurrent neural networks (RNN). Although the model can perform quite well on the material points with similar geometric features as the training database, it has limited transferability to complex geometries, where the geometric feature and the state of the boundaries are different from those of the trained material points. Stathatos and Vosniakos (2019) proposed a custom scanning path decomposition method and used artificial neural networks (ANN) to predict the evolution of temperature for arbitrary long paths in laser-based additive manufacturing (LBAM). However, the model was only demonstrated on the prediction of the thermal field of a single layer AM model. Paul et al. (2019) utilized extremely randomized trees (ERT) and an ensemble of bagged decision trees as the regression algorithm for real-time prediction of thermal profiles in the DED process. In the model, the temperatures of prior voxels and laser information are used as inputs to predict temperatures of subsequent voxels. The model achieved MAPE below 1%. However, as the ML model utilized a feature set relying on neighboring voxels with a uniform mesh of rectangular elements, the model would need to be modified to generalize for irregular geometries and meshes. Ren et al. (2020) introduced a physics-based ML model that utilized deep neural networks (DNNs) combining RNNs to build the relationship between scanning patterns and the corresponding thermal field. This model achieved a prediction accuracy of more than 95% on arbitrary scanning patterns and geometries. However, it was only demonstrated on a single layer. To address these problems, Zhou et al. (2021) proposed a 3D corrected matrix to describe the cube-mesh-based laser deposition status and used it as inputs in an RNN&DNN model. The model performed well on a wide variety of geometries and deposition patterns. However, as the curved edges cannot be meshed into perfect cubic cells, the deposition state of the mesh near the edge cannot be accurately represented by the units of

Table 1
Summary of the existing ML models for thermal prediction in AM, where T is temperature.

Paper	Year	Process	Model	Predicted value	Dataset size
Mozaffar et al. (2018)	2018	DED	RNN	Stepwise nodal T	250,000
Paul et al. (2019)	2019	DED	ERT	Ts of subsequent voxels	9.05 million
Stathatos and Vosniakos (2019)	2019	LBAM	ANN	Sequence of local Ts	54,450
Ren et al. (2020)	2020	LBAM	RNN	Laser deposition matrix	47,152
Roy and Wodo (2020)	2020	FDM	ANN	T profile coefficients	12,000
Roy and Wodo (2021)	2021	FDM	ANN	Consolidation degree	87,800
Pham et al. (2021)	2021	DED	FFNN	Stepwise nodal T	19.9 million
Fetni et al. (2021)	2021	DED	ANN	Stepwise nodal T	4 million
Zhou et al. (2021)	2021	DED	RNN	T state data	98,585

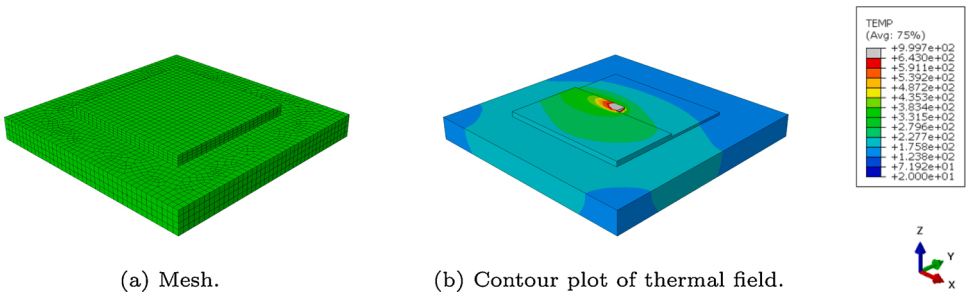

(a) Mesh. (b) Contour plot of thermal field.

Fig. 1. FE models generated in the work. (a) The FE mesh. (b) The FE thermal field during deposition of Case 1 (as described in Table 2).

the 3D matrix. Hence, it can be expected that the prediction accuracy of the nodes near the curved edge will be affected. Besides, because the size of the 3D input matrix determines the number of all cells in the model, the size of the predictable AM parts is limited by the size of the input matrix.

It is also worth noting that the alternative models mentioned above (Mozaffar et al., 2018; Paul et al., 2019; Ren et al., 2020; Stathatos and Vosniakos, 2019; Zhou et al., 2021) either rely on a large amount of data to learn the correlations between high-dimensional inputs and outputs or focus on specific cases with low dimensional inputs and outputs. In order to address this problem, some physical-based ML models (Fetni et al., 2021; Pham et al., 2021; Roy and Wodo, 2020, 2021; Zhou et al., 2021) have been developed by using input features that can characterize the physical processes occurring in various AM models or manufacturing processes. Roy and Wodo (2020) proposed a set of distance-based features by incorporating the characteristics of the thermal processes in fused deposition modeling (FDM) and built a neural network model that required smaller datasets compared to the ML models proposed in Mozaffar et al. (2018), Paul et al. (2019), Ren et al. (2020), and Stathatos and Vosniakos (2019). The ML model had a short training time and achieved a competitive accuracy, making the ML model well suited for in situ approximations. However, due to non-generic features based on the distance from cooling surfaces, the ML model was only suitable for simple, rectangular geometries. Roy and Wodo (2021) addressed the challenges in Roy and Wodo (2020) and optimized the physics-based feature set and output. The proposed ML model is applicable for different structures, but some of the proposed features are dependent on the seeding in the FEM mesh, meaning that the features will have limited transferability to complex geometries, where the element size is usually not homogeneous. Fetni et al. (2021) proposed a set of input features characterizing the positions of calculated point and laser heat source, and deposition time and trained an ANN model to reproduce the temperature fields in DED. Pham et al. (2021) introduced the input energy and the number of current printing layer to Fetni et al.'s feature set and utilized feed-forward neural networks (FFNN) to predict the thermal profile. Both models achieve prediction accuracy of more than 99%. However, the geometric feature and the state of the boundaries are not considered in these models. Therefore, they are only applicable for samples with simple geometric shapes.

As illustrated, the current state-of-the-art has established the fundamental framework of ML predictions of thermal fields. Although, some ML models have good performance in thermal prediction of specific cases, the scope of these ML models is still limited by non-generic features that are unable to handle varying simulation properties. The proposed approach in this work addresses this problem by developing a generic feature set that captures the thermal processes without relying on simplifications of the parts.

3. Data generation

In this section, the procedure for dataset generation with FE simulations will be outlined. In addition, the characteristics of the performed simulations will be highlighted. In order to generate the datasets for training and testing in the ML model, finite element simulations are performed with ABAQUS software and the Additive Manufacturing module. For all simulations, the wire arc additive manufacturing process is studied, and the pass width and layer thickness are 10 mm and 2.23 mm, respectively. The material of the substrate and deposited parts is aluminum alloy 2319 (AA2319). The density is 2823 kg/m^3. The liquidus temperature and solidus temperature are 643 °C and 543 °C, respectively.

In the FE models, a double-ellipsoid heat source model is utilized and

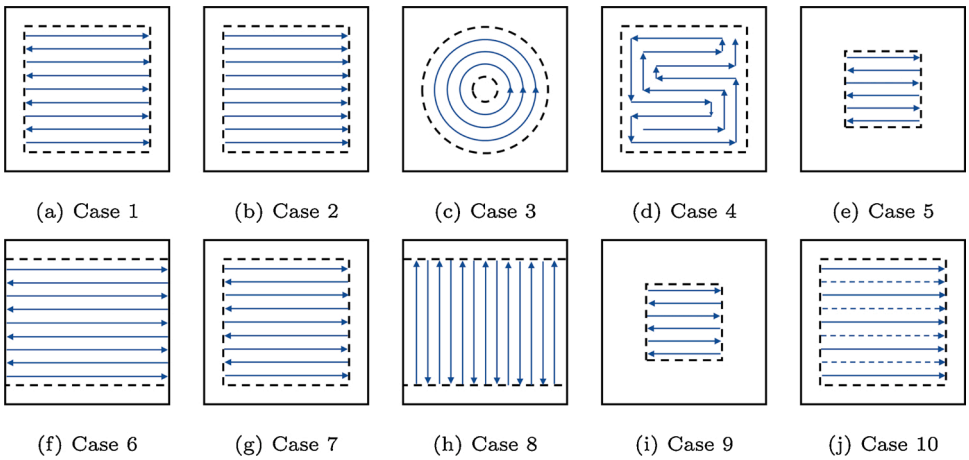

(a) Case 1 (b) Case 2 (c) Case 3 (d) Case 4 (e) Case 5

(f) Case 6 (g) Case 7 (h) Case 8 (i) Case 9 (j) Case 10

Fig. 2. Illustrations of geometry and deposition patterns of all simulations in the full dataset. The black lines indicate the base, the black dashed lines indicate the deposition geometry, and the blue arrows indicate the direction of the laser.

Table 2
Simulation summary. All Cases have 4 layers except for Case 9 (marked with *) which have 10 layers.

Case	Q (kw)	Dimensions (m^3)	Samples	Elements	Pattern
1	5	0.12 * 0.12 * 0.0092	946,015	9600	ZigZag
2	5	0.12 * 0.12 * 0.0092	1,205,341	9600	Raster
3	5	π * 0.12^2*0.0092	2,279,859	9672	Out-in spiral
4	5	0.12 * 0.12 * 0.0092	1,681,543	9600	S
5	5	0.06 * 0.06 * 0.0092	80,504	8148	ZigZag
6	5	0.12 * 0.16 * 0.0092	935,566	9812	ZigZag
7	5-4	0.12 * 0.12 * 0.0092	1,083,363	9600	ZigZag
8	5	0.12 * 0.16 * 0.0092	2,402,788	9812	ZigZag
9*	5-2	0.06 * 0.06 * 0.0230	470,591	9012	ZigZag
10	5	0.12 * 0.12 * 0.0092	1,286,788	9600	Alternate-line

Table 3
Introduction of the features used in the machine learning model.

Feature name	Feature description
t	Sample time (s)
t_i	Deposition time of node (s)
n	Boolean value that define whether or not the adjacent pass or layer is printed at the given time
t_n	Time since the adjacent nodes were deposited (normalized by the velocity) (m)
t_{HIZ}	Time since the node was in the heat influence zone (HIZ) (normalized by velocity) (m)
d_e	Euclidean distance between nodal position and laser position (m)
P_{inf}	Power influence (Eq. (7)) ($\frac{J}{m^3}$)
VR	Volume ratio

the value of the related parameters are presented in Appendix A. The element type used in the FE model is 8-node linear heat transfer brick (DC3D8). In thermal analysis, thermal conductivity, thermal convection, and radiation are considered. The thermal property parameters are provided in Appendix A. Both the initial temperature of the substrate and the ambient temperature is 20 °C. The deposition speed is 10 mm/s. The elements and materials properties are activated at the appropriate time based on the deposition sequence under different patterns. After deposition, the model naturally cools down to room temperature.

The datasets include data samples from several finite element simulations with varying deposition patterns, dimensions, geometries, power input intensities, and other process parameters. This has been done in order to explore the transferability of the extracted feature space and ML model on several cases. An example of the generated FE models can be seen in Fig. 1 and an overview of the different geometries and deposition patterns of the simulations can be seen in Fig. 2. The variables of the simulations can be seen in Table 2, and the rest of the simulation properties, which are constant for all simulations, can be seen in Appendix A.

Each data sample in the datasets represents the transient properties of a node at a specific time. All simulations were run with the inactive activation strategy, meaning that the elements representing the deposited material are not considered until the material is deposited and the element is activated (Gouge and Michaleris, 2017). This implies that the dataset only contains data samples from activated elements and that the elements in the base is not included in the dataset. Each sample includes information about the time and the nodal and laser position. In addition, the nodal temperature, T, has been added, which means that the dataset is labeled and therefore suited for supervised learning. All simulations were sampled at the simulation increments, meaning that the samples are not uniformly distributed in time.

The preprocessed datasets are publicly available at: https://cutt.ly/QnqXV9Z.

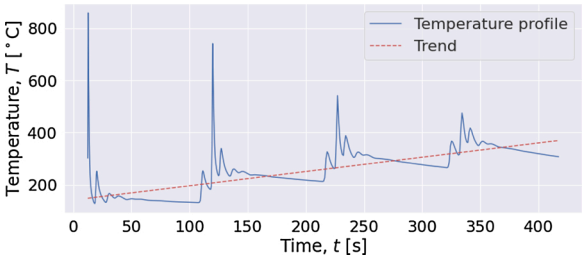

Fig. 3. Thermal profile of an internal node in the first layer of Case 1 illustrating heat accumulation during deposition in AM.

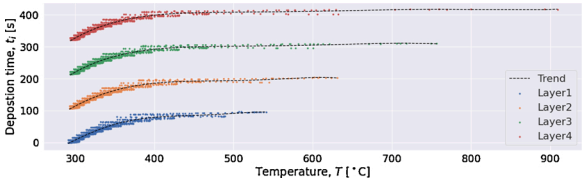

Fig. 4. Scatter plot illustrating relationship between the deposition time t_i and the temperature T for all nodes at the last timestep of the deposition process ($t \approx 417$ s) of Case 1.

4. Feature engineering

Here we highlight the feature engineering performed in this work, which comprises techniques to clean and organize data for machine learning pipelines (Ozdemir and Susarla, 2018). Domain knowledge has been applied to extract features from raw data so that it was able to represent the problem at hand better, which is important as good feature engineering leads to increased ML model performance (Ozdemir and Susarla, 2018; Kourou et al., 2015). In this case, a generic feature space has been extracted from the raw data generated by FEA. The features have been extracted based on the underlying physics of the thermal processes in AM. In contrast to features proposed in previous works (Paul et al., 2019; Mozaffar et al., 2018; Roy and Wodo, 2021, 2020; Ren et al., 2020; Zhou et al., 2021), the feature space is not dependent on simulation specific properties, meaning that it does not require alterations for handling simulations with different geometries, meshes, deposition properties, or boundary conditions. The feature space is presented in Table 3, and the features and their theoretical background will be described in this section.

4.1. Sample time, t

t is the time when the sample is extracted, where $t = 0$ is the time when the simulation started. This is relevant as the heat input in additive manufacturing processes causes heat accumulation, which leads to a progressive increase of the average workpiece temperature during the printing process. The correlation of increased average workpiece temperature is illustrated in Fig. 3 and further supported by the partial dependence plot in Fig. C.13d.

4.2. Deposition time, t_i

t_i is the time when the sampled node was activated in the FE model, which corresponds to the time when the node was deposited. As the trend lines in Fig. 4 illustrates, the deposition time has a clear relationship with the temperature. The data samples of each layer are separated and demonstrate similar trends.

4.3. Euclidean distance, d_e

The nodal temperature increases when the laser approaches the node

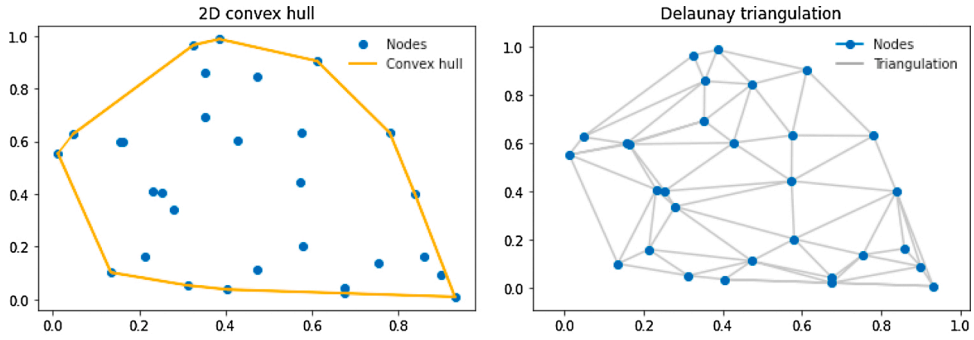

(a) Illustration of 2D convex hull. (b) Illustration of Delaunay triangulation.

Fig. 5. Illustration of convex hull and Delaunay triangulation used for calculation of active volume within HIZ.

and decreases when the laser moves away from the node, which can be observed when the thermal profiles of nodes are studied. An example of such a thermal profile can be seen in Fig. 3, where the thermal profile of an internal node in the first layer in Case 1 has been plotted. The graph shows a cyclic reheating pattern with four reheating periods, each heating cycle corresponding to one deposited layer. Each reheating period consists of a reheating peak, where the absolute distance to the heat source is minimal for the given deposited layer. In addition, each reheating period inhibits oscillations that correspond to the passes of the laser. The absolute value of the peaks in each cycle is decreasing for each deposited layer, indicating a direct relationship between the nodal temperature and the distance to the heat source. The Euclidean distance, d_e, is used to represent the distance between the laser and the sample node, and is expressed in Eq. (1). The equation gives the length of a line segment between two points $\mathbf{X} = (x_1, x_2, \ldots, x_n)$ and $\mathrm{Y} = (y_1, y_2, \ldots, y_n) \in \mathbb{R}^n$, and is the most common distance metric used in ML (James et al., 2014). In this project, the Euclidean distance in 3D has been applied, giving $n = 3$.

$$d_e(\mathrm{X}, \mathrm{Y}) = \left(\sum_{i=1}^{n} (x_i - y_i)^2 \right)^{\frac{1}{2}} \tag{1}$$

4.4. Boolean value of deposition of adjacent node, n

The Euclidean distance is further used to extract the feature n. The feature n is a boolean value that defines whether or not the adjacent pass or layer is printed at the given time. The boolean value is found by checking if the laser is further away than the pass width, a, as indicated in Eq. (2). The primary oscillations in the thermal profiles occur when the neighboring elements are deposited, and n will capture this. Although n is dependent on the Euclidean distance d_e, the feature still refines the predictions due the random cuts and feature sampling performed in extra trees predictions.

$$n = \begin{cases} \text{True} & \text{if } d_e \leq a \\ \text{False} & \text{if } d_e > a \end{cases} \tag{2}$$

4.5. Normalized time since adjacent node deposition, t_n

t_n has been added to capture the heat accumulation and cooling after the laser has been in close vicinity to the given node. t_n gives the time since one of the neighboring nodes was deposited as seen in Eq. (3), where Δt is the time since the previous time step and t_{prev} is the time interval since the condition was last satisfied. The feature is normalized with the velocity, v, to make it more generic.

$$t_n = \begin{cases} 0 & \text{if } d_e \leq a \\ \dfrac{\Delta t + t_{\text{prev}}}{v} & \text{if } d_e > a \end{cases} \tag{3}$$

4.6. Normalized time since deposition within heat influence zone (HIZ), t_{HIZ}

t_{HIZ} denotes the time since the laser was within the nodal heat influence zone (HIZ), as seen in Eq. (4), where Δt is the time since the previous timestep and t_{prev} is the time interval since the condition was satisfied. Note that this is not necessarily the same value as t_{prev} in Eq. (3). The feature is normalized with the velocity, v, to make it more generic. The HIZ was defined by Roy and Wodo (2020) to be the spatial region where a minimum thermal change occurs and where the first-order thermal effects are dominant. Roy and Wodo (2020) calculated the size of the HIZ by the analytical solution to the transient heat equation with a point source on a semi-infinite body. However, Sun et al. (2021, 2019) observed that the heat input had minor influence outside a hemisphere with the heat input as the center and a radius of $r = 3a$, where a is the pass width, and this can therefore be used as a good approximation for the HIZ. t_{HIZ} is therefore indicating how long it is since the laser was in close enough proximity to the node to have a significant impact on the nodal temperature.

$$t_{\text{HIZ}} = \begin{cases} 0 & \text{if } d_e \leq 3a \\ \dfrac{\Delta t + t_{\text{prev}}}{v} & \text{if } d_e > 3a \end{cases} \tag{4}$$

Both t_n and t_{HIZ} have been added to capture the heat accumulation and cooling after the laser has been in close vicinity to the node and is inspired by the three pattern features presented by Roy and Wodo (2021). However, the features in this work have been made more concise, and the two features t_n and t_{HIZ} are proposed as an alternative with lower dimensionality.

4.7. Power influence, P_{inf}

The influence of the laser on the thermal profiles of nodes is covered by the power influence feature, P_{inf}. Similar to some features presented by Roy and Wodo (2021), P_{inf} is an equation inspired by the analytical solution of the transient heat equation in 3 dimensions. The transient heat equation is a partial differential equation that represents the heat diffusion in the part and is defined by Eq. (5), where α is the diffusivity.

$$\frac{\partial T}{\partial t} = \alpha \left(\frac{\partial^2 T}{\partial^2 x} + \frac{\partial^2 T}{\partial^2 y} + \frac{\partial^2 T}{\partial^2 z} \right) = \alpha \nabla^2 T \tag{5}$$

The analytical solution of Eq. (5) for an instantaneous point heat source (Q) on an infinite medium is given by Eq. (6), as defined in Carslaw and Jaeger (1959).

$$\Delta T(d, t) = \frac{Q}{(4\pi\alpha t)^{\frac{3}{2}}} \exp\left(-\frac{d_e^2}{4\alpha t} \right) \tag{6}$$

The extracted feature P_{inf} is given by Eq. (7), where P_ρ is the power

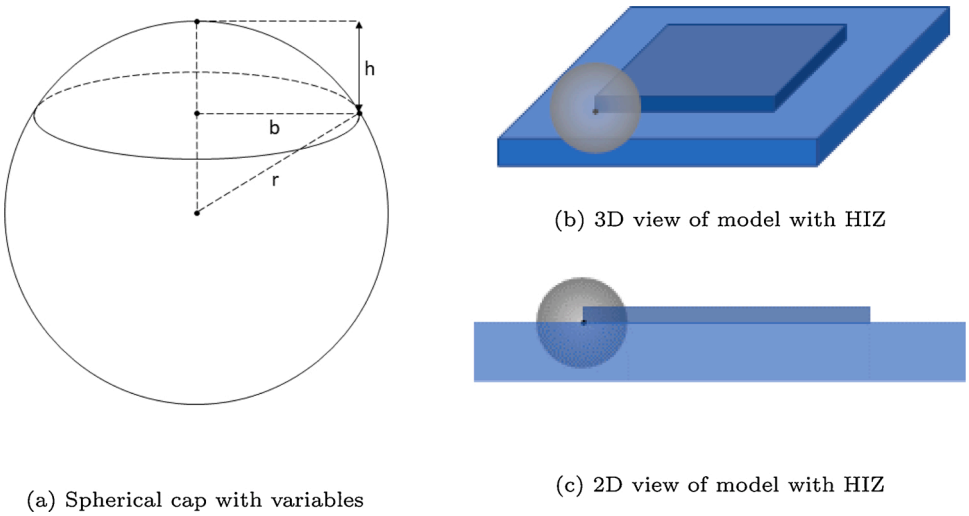

(a) Spherical cap with variables

(b) 3D view of model with HIZ

(c) 2D view of model with HIZ

Fig. 6. Illustration of spherical cap and part with an indication of node (black dot) and HIZ (grey sphere). The dark blue area is the deposited material, and the light blue area is the base. The spherical cap is used to calculate the base volume within the HIZ.

density as given in Eq. (8), where A is the bead area of the deposited material and v is the deposition velocity. P_ρ gives the amount of transferred power per unit volume and takes into account the fact that heat accumulation is velocity-dependent. P_{inf} is a simplification of Eq. (6) and aims to capture that the influence of the heat source is inversely correlated with the distance. The Euclidean distance, d_e, is normalized with the pass width, a, to get a dimensionless exponential.

$$P_{\text{inf}} = P_\rho \exp\left(-\frac{d_e^2}{a^2}\right) \tag{7}$$

$$P_\rho = \frac{Q}{\text{Av}} \tag{8}$$

4.8. Volume ratio, VR

The feature *VR* was extracted to capture the thermal loss from convection and radiation on the evolving free surfaces. *VR* indicates how much of the HIZ around a node is filled with air, which is related to the amount of convection through free surfaces nearby the node. *VR* is calculated with Eq. (9), where V_{HIZ} is the approximated volume surrounding the of active nodes within the nodal HIZ, V_{base} is the volume of the base within the HIZ, and V_{tot} is the total volume of the HIZ. A low value of *VR* would mean that the node is close to a surface, and cooling due to convection to the surrounding air will occur.

$$\text{VR} = \frac{V_{\text{HIZ}} + V_{\text{base}}}{V_{\text{tot}}} \tag{9}$$

V_{HIZ} is calculated by calculating the volume of the 3D convex hull around the active nodes in the HIZ. A convex hull of a set of points is the smallest convex set that contains the points, which is illustrated in Fig. 5a. A set, $C \subseteq \mathbb{R}^n$ is defined as convex if for all points $p \in C$, the line segment connecting two points, p_i and p_j where $i \neq j$, is included in C (Berman and Paul, 2005).The algorithm used is Quickhull, which is optimal for point clouds with uniform point distribution (Barber et al., 1996). By utilizing the convex hull and not the nodes, as was done in Roy and Wodo (2021), *VR* is independent of the element size in the mesh. In order to calculate the volume of the convex hull, triangulation was performed. Triangulation of a set of points C is a simplistic decomposition of the convex hull of C (o'Rourke, 1998). In 3 dimensions, triangulation of C means decomposing the convex hull into tetrahedra. In this work, Delaunay triangulation has been performed, as illustrated in Fig. 5b.

The volume of the HIZ is calculated using the equation for a sphere with radius r, as in Eq. (10). To calculate the volume of the base inside the HIZ, the equation for a spherical cap is used. The equation for a spherical cap is given in Eq. (11), where h is r minus the difference of the nodal z coordinate and the height of the base, h_b, $h = 3a - (z - h_b)$. A sphere with a spherical cap is illustrated with the relevant variables in Fig. 6a.

$$V_{\text{tot}} = \frac{4}{3}\pi r^3 \tag{10}$$

$$V_{\text{base}} = \frac{\pi h^2}{3}(3r - h) \tag{11}$$

5. Machine learning modeling

The features have been developed based on the thermal behavior in additive manufacturing processes and are simulation independent, making them possible to apply for thermal predictions of computational models with a different thermal nature. The features have been tested and validated through machine learning experiments.

Paul et al. (2019) found that among several tested regression methods, extremely randomized tree, commonly known as extra trees (ERT), had the best performance. As the focus of this work was to improve performance and generalizability by improving the features, not the ML model, the same ML approach as in Paul et al. (2019) was chosen. ERT is a tree-based method that ensembles several decision trees, which implies a non-linear algorithm that involves stratification of the feature space. When the feature space is segmented into simple regions, predictions can be made based on the samples in each region (James et al., 2014; Mitchell, 1997; Géron, 2019). ERT are advantageous due to their simplicity, speed, interpretability, and robustness to mixed and noisy data. In addition, they tend to handle big datasets well, and among tree-based methods, ERTs have one of the highest computational efficiencies while still achieving a competitive accuracy (Géron, 2019; Geurts et al., 2006). In order to achieve a competitive level of predictive accuracy, one generally has to aggregate methods with several trees to achieve a competitive performance to other advanced ML methods such as neural networks, and the ideal number may be found through

Table 4
Correlation with target value, T.

Feature name	Spearman	Pearson
t	0.77	0.64
t_i	0.42	0.42
d_e	−0.29	−0.34
P_{inf}	0.31	0.37
VR	0.11	−0.22
n	0.27	0.25
t_n	0.30	0.27
t_{HIZ}	−0.28	−0.18

techniques such as grid search (James et al., 2014; Liashchynskyi and Liashchynskyi, 2019). In our work, the ERT models consists of 55 trees. The number of trees was set to 55 based on a grid search and was a trade-off between accuracy and processing time.

6. Results

In this section, the experimental results for the data-driven ML-based control system will be presented, along with an evaluation of the developed features. Furthermore, the results that demonstrate the generalizability of the ML models will be presented. All ML models aggregate 55 extremely randomized trees. The performance of the train set is assessed through the average of the 5-fold cross-validation results, an iterative procedure where the entire dataset is randomly partitioned into five disjoint subsets of approximately the same size. For each partitioning of the dataset, the performance of the given split is measured. The cross-validated train errors are measured with the mean absolute error (MAE) and then averaged to indicate the test performance. The metrics MAE, the mean absolute percentage error (MAPE), and the root mean squared error (RMSE) are utilized to measure test performance. Note that low values of MAE, MAPE, and RMSE indicate high performance. MAPE will mainly be utilized to discuss the test performance. However, all three metrics are added to demonstrate that the metrics, which have different strengths, are consistent.

6.1. Feature evaluation

In order to evaluate the performance of the proposed features, three properties have been investigated; correlation, permutation feature importance, and partial dependence. To perform the feature evaluation, the datasets from Cases 1, 2, and 7 were combined. The rest of the datasets were not utilized to ensure that some of the data is previously unseen. In addition, an extra-tree model was constructed to calculate the permutation feature importance and partial dependence. The partial dependence plots (PDP) displayed the expected and wanted response, as described when the features were introduced earlier in this section, and can be seen in Appendix B.

6.1.1. Correlation

Correlation indicates dependence and whether there exists any statistical relationship between two variables (Lee Rodgers and Nicewander, 1988). Several coefficients measure correlations, but the most common of these is the Pearson correlation coefficient. The Pearson correlation coefficient, r_P, indicates whether or not there exists a linear relationship between two variables (Pearson, 1896). In addition, the Spearman correlation coefficient, r_S, is often investigated to identify nonlinear relationships between two variables (Spearman, 1904). The correlation coefficients give a value between −1 and 1, where −1 and 1 indicate full negative and positive correlation respectively, and 0 indicates no relationship (James et al., 2014).

The Pearson and Spearman correlation has been calculated to ensure a predictive relationship with the output variable, T. As seen in Table 4, all features have a predictive relationship with T. It can also be noted that the feature t has the highest values of r_P and r_S, and is strongly correlating with T.

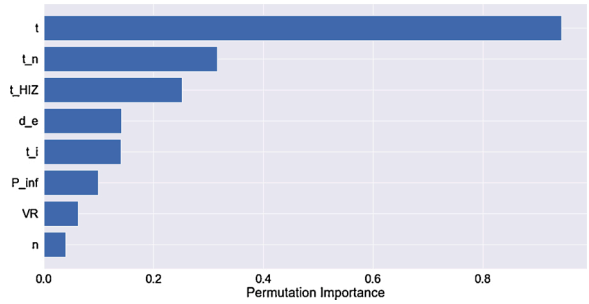

Fig. 7. Permutation feature importance of feature space.

Table 5
Results of investigations of baseline performance.

Case Nr.	Train	Test		
	MAE	MAE	MAPE	RMSE
1	2.081	3.929	1.228	15.229
2	2.620	2.510	0.793	9.367
3	4.884	4.676	1.408	18.621
4	4.865	4.597	1.156	17.459
5	12.322	11.882	4.653	28.409
6	2.969	2.684	0.909	10.971
7	3.279	3.039	1.035	10.853
8	2.863	2.645	0.800	11.970
9	7.084	6.565	2.452	20.796
10	3.291	3.013	0.954	13.934

6.1.2. Permutation feature importance

Permutation feature importance is commonly used to rank features based on the importance of the feature. The measure is defined to be the decrease in the ML model performance if the column values of a feature are randomly shuffled (Breiman, 2001; Altmann et al., 2010). The random shuffling of the column values breaks the relationship between the feature and the ML model and indicates how much the ML model depends on the feature.

The permutation feature importance of this feature space is illustrated in Fig. 7. As with the correlation results, it can be seen that the feature t has the highest feature importance. In addition, it can be seen that all features influence the predictions. The two features n and VR have permutation feature importance values below 0.1, which is not very high. However, both features target outlier data samples and will not be significant on average but still crucial for specific data samples. VR is necessary for nodes with a different rate of convection due to free

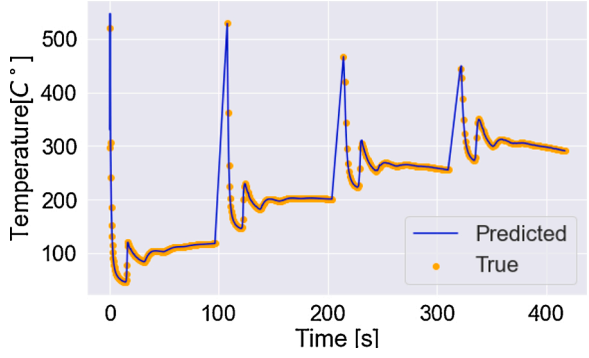

Fig. 8. True and predicted thermal field of corner node with coordinates (−0.01, − 0.045, 0.0223) in Case 1.

Table 6
Layer transferability with Case 9. The geometry of the FE model is quadratic with 10 layers and was deposited with ZigZag pattern.

	Train	Test		
	MAE	MAE	MAPE	RMSE
9-1	19.997	2.923	5.808	20.976
8-2	21.014	13.641	5.961	23.254
7-3	23.310	16.286	6.959	26.432
6-4	25.602	21.702	9.123	35.469

surface. However, most nodes are internal and have the same value of *VR*. Similarly, *n* is only *True* for very few samples, and one would therefore not expect the feature to have high importance on average.

6.2. Baseline performance

This section demonstrates the overall capability of the features and the ML models, denoted baseline performance in this paper. A ML model's baseline performance is that it generalizes well on data samples from the same simulation as the ML model was trained on. The generalizability of the ML models will be further assessed in the following subsections.

As the baseline performance predicts temperatures from the same simulation, the train set that the ML model was trained on perfectly captures the conditions in the test set. The high performance demonstrates that the features can capture the thermal processes in additive manufacturing if the ML model at hand is trained at a suitable dataset. In addition, the results demonstrate that the features are generic as the ML models were tested on cases with varying geometries, deposition patterns, power intensities, and meshes.

The baseline performance has been tested on all 10 simulations that were presented in Fig. 2, meaning that a wide range of simulation characteristics has been tested. All simulation datasets were split into two sets; the train (80% of the samples) and the test set (20% of the samples). The results are presented in Table 5 and indicate high baseline performance, where all cases except Case 5 had a MAPE below 2.5%. The predicted values are compared with the original FE data samples of a corner node in Case 1 in Fig. 8, which demonstrates that the deviation between the predicted and true value is small. Case 5 has 80,504 samples, which is by far the smallest dataset tested in this work, and the low performance for this case is therefore not surprising.

6.3. Layer transferability

Layer transferability addresses whether or not the ML model can predict the future thermal history of the case that it was trained on. In this work, the datasets have been split when a layer is wholly deposited, generating one dataset per deposited layer. It is important to note that the simulation cost grows exponentially with the number of layers and size of the part geometry. Therefore, the utility of having layer transferability would be to reduce computational time by simulating some of the deposited layers and then using the generated data to train a ML model that may predict the successive layers.

Case 9 was used to investigate the ML model's capacity to predict future temperatures if trained on an earlier time interval. Case 9 has 10 layers, and the datasets utilized for training and testing the ML models were split based on the time intervals where each layer was deposited. Four configurations were tested; after the sixth (denoted *6-4*), seventh (denoted *7-3*), eighth (denoted *8-2* and ninth layer (denoted *9-1*) was deposited. For example, *9-1* means that the time interval when the last layer is deposited is predicted based on the time interval of the first nine deposited layers. The results are presented in Table 6, and each configuration is illustrated with plots of nodal thermal history in Fig. 9. The limits of the train and test sets are indicated as the dataset limits in each plot.

As expected, the predictions are performing better with fewer layers to predict. Configuration *9-1* performs the best with a MAPE of 5.808%. The percentage is low enough to give a realistic impression of the nodal thermal history, which also can be observed in Fig. 9d, where the predicted and true values are similar. Configuration *6-4* has the worst

Table 7
Results of pattern transferability.

Case Nr.		Train	Test		
Train	Test	MAE	MAE	MAPE	RMSE
1	2	25.180	13.736	4.955	28.047
2	1	26.206	13.231	4.540	28.475
1	4	57.699	44.830	12.601	74.268
2	4	26.206	60.824	16.430	88.815
6	8	20.231	18.627	7.597	27.099
8	6	2.863	19.532	8.306	30.326
2	10	26.206	55.914	24.713	76.494
4	10	38.574	58.985	25.728	75.605

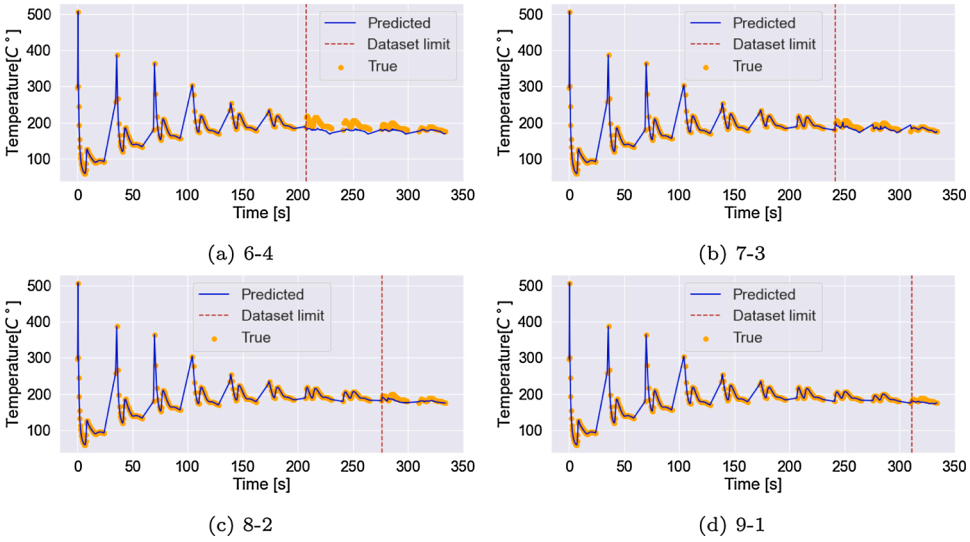

(a) 6-4 (b) 7-3

(c) 8-2 (d) 9-1

Fig. 9. True and predicted thermal field of corner node with coordinates (−0.03, − 0.03, 0.0223) in Case 9. The plots illustrate the layer transferability of the ML model.

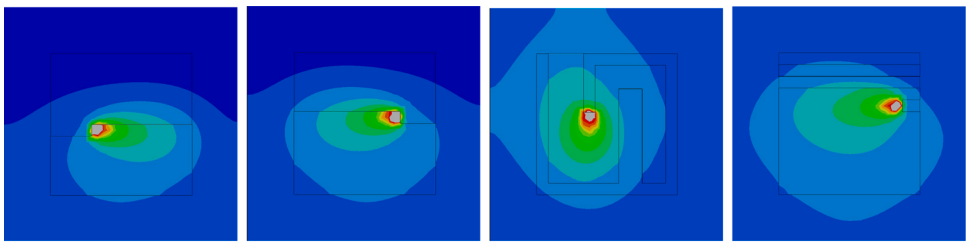

(a) ZigZag (b) Raster (c) S (d) Alternate-line

Fig. 10. Thermal fields of selected FE models with varying deposition patterns while depositing the first layer.

Table 8
Results of investigations of power intensity transferability.

Case Nr.		Train	Test		
Train	Test	MAE	MAE	MAPE	RMSE
7	1	20.181	28.729	9.933	44.956
1	7	25.180	20.323	7.671	31.977

Table 9
Combined simulation-to-simulation predictions.

Case Nr.		Train	Test		
Train	Test	MAE	MAE	MAPE	RMSE
5 + 6	1	53.634	29.187	10.215	45.884
5 + 6 + 2	1	3.162	13.645	4.631	27.909
1 + 3 + 4	10	4.532	28.127	12.292	41.649
1 + 4	2	5.405	15.322	5.590	32.523
2 + 4	1	61.988	13.431	4.674	28.723
1 + 7	9	22.785	33.693	11.046	51.217

performance with a MAPE of 9.123%, which is not sufficient for realistic optimization. A probable reason for the decreasing performance is that the number of samples in the train set decreases. Configuration *6-4* has a training dataset of 168,194 samples, which is significantly lower than 427,718 samples in configuration *9-1*.

6.4. Pattern transferability

Another investigated scenario is pattern transferability. When investigating pattern transferability, the question at hand is whether or not the trained ML model performs well on different patterns than it was trained on. Pattern transferability gives flexibility to the ML model as this allows reusing datasets, which means that a previously generated dataset from a FE model can predict the thermal history of a new FE model with a different deposition pattern.

Pattern transferability was investigated by training and testing ML models on datasets where the simulation parameters are identical except for the deposition pattern. The results are presented in Table 7, where it is evident that the variability in the results is considerable, ranging from MAPE of 4.540% and 25.728%. The best results were achieved when FE models with the deposition patterns ZigZag and Raster predicted each other. These results are not surprising as the two patterns are similar, having the same vector length and similar thermal fields, as seen in Fig. 10. The ML models where Cases 6 and 8 predict each other also have a relatively low MAPE of 7.597% and 8.306%. The two cases are rectangular and deposited with ZigZag, but the deposition direction is different, giving different vector lengths. This indicates that the feature space has transferability with different vector lengths. The worst result appeared when Case 10 was predicted by Case 4 with MAPE of 25.728% and RMSE of 74.268. Case 4 is a quadratic part deposited with S pattern, a novel pattern introduced by Sun et al. (2021). The pattern has a changing deposition direction and vector length which generates a more uniform thermal field. This is illustrated in Fig. 10 where the thermal field of the S pattern has a significantly different thermal distribution from the deposition pattern of Case 10, Alternate-line. The temperature of the part is overall higher, and the region with high temperatures (colors around the grey melt pool) is more extensive than Case 1. This shows that the S pattern gives a more uniform thermal field and lower thermal gradients. Due to the difference in thermal fields, it is not surprising that the pattern transferability between the S pattern and ZigZag is low.

6.5. Power intensity transferability

The power intensity transferability addresses whether ML models trained on one load condition may predict data from simulations with different load conditions. Similar to pattern transferability, this gives flexibility when training ML models.

Power intensity transferability was investigated by training and testing ML models on Cases 1 and 7. The two cases are identical except that Case 1 does not have power intensity reduction, while Case 7 has 5% intensity reduction per deposited layer. The results can be seen in Table 8, where training on Case 1 and testing on Case 7 works the best with a MAPE of 7.671%. Training on Case 7 and testing on Case 1 gives a bit higher MAPE of 9.933%. The complete thermal history of a corner

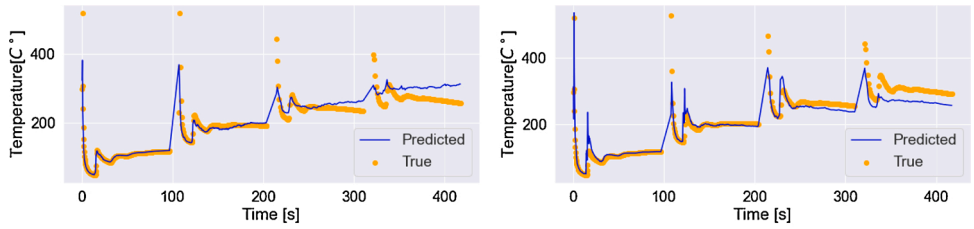

(a) Train: Case 1, Test: Case 7 (b) Train: Case 7, Test: Case 1

Fig. 11. True and predicted thermal field of corner node with coordinates (−0.06, − 0.06, 0.0223) in Case 7. The plots illustrate power intensity transferability.

Table 10
Comparison of the performance of this model and others' ML-based models. Note: Category of the dataset volume, (a) large: more than 1 million; (2) medium: between 100,000 and 1 million; (3) small: less than 100,000.

Models	Transferability					Dataset
	Geometry	Layer	Pattern	Power	Mesh	Size
Mozaffar et al. (2018)	Simple	Yes	Yes	Yes	Yes	Medium
Paul et al. (2019)	Simple	Yes	Yes	No	No	Large
Stathatos and Vosniakos (2019)	Single layer	No	Yes	No	Yes	Small
Ren et al. (2020)	Single layer	No	Yes	No	No	Small
Roy and Wodo (2020)	Simple	Yes	No	No	Yes	Small
Roy and Wodo (2021)	Simple	Yes	Yes	No	No	Small
Pham et al. (2021)	Simple	Yes	Yes	Yes	Yes	Large
Fetni et al. (2021)	Simple	Yes	Yes	No	Yes	Large
Zhou et al. (2021)	Smaller than the trained models	Yes	Yes	No	No	Small
This work	Yes	Yes	Yes	Yes	Yes	Small

node from the original FE simulation is presented along with the ML predictions in Fig. 11. The results demonstrate that both configurations capture the general trend but are struggling with the peaks. A high RMSE confirms this compared to what is expected based on the MAE and MAPE values.

6.6. Combined simulation-to-simulation predictions

The combined simulation-to-simulation predictions are predictions made with ML models that are trained on datasets from several cases. By exposing the ML model to different thermal states, the likelihood of overfitting is reduced, and the likelihood of transferability increases. Several cases have been investigated, where cases with different characteristics have been combined to train and predict data from other simulations than what it was trained on.

The results are presented in Table 9, and are in general free from overfitting with test errors that are not significantly higher than the train errors. In addition, the test errors are, in general, lower than for the ML models only trained on data from one case. This is because the ML model has been exposed to data samples that are influenced by different thermal processes, which enables the model to make more unbiased predictions.

A ML model was trained on Cases 5 and 6 and tested on Case 1, where Case 5 is a smaller version of Case 1 and Case 6 is a longer version of Case 1. The ML model trained on Cases 5 and 6 achieved a MAPE of 10.215% when predicting Case 1. The results are significant as a case with a different geometry than what the ML model was trained on was predicted.

The results of the ML model trained on Cases 1, 3, and 4 predicted Case 10 with a MAPE of 12.292% should also be noted. Case 10 is deposited with the pattern alternate-line, one of the patterns with a complex thermal field, and is comparable with the prediction of Case 4 presented in Section 6.4, which achieved a MAPE of 12.601%. The difference in MAPE is not significant, but there is a significant improvement in adjusted RMSE, which indicates that the model captures more variability and has fewer outliers in its predictions.

We can also observe that the model trained on Cases 1 and 7 permits transferability of both power intensity and geometry when datasets are combined for ML model training. This model predict Case 9 with a MAPE of 11.046%, where Cases 1 and 7 are quadratic with layer area of $0.12 * 0.12\ m^2$ and have four layers. Case 9 is also quadratic but with ten layers and a significantly smaller layer area of $0.06 * 0.06\ m^2$. In addition, the laser intensity is also different in all cases. The good results indicate transferability both in power intensity and geometry when datasets are combined for ML model training.

6.7. Overall evaluation

Among the results obtained in this work, the baseline performance is the highest, with MAPE values ranging from 0.793% to 4.653%. As the baseline performance predicts temperatures from the same simulation as it was trained on, the train set that the ML model was trained on perfectly captures the conditions in the test set. Therefore, these results show that the features can capture the thermal processes in additive manufacturing if the ML model at hand is trained at a suitable dataset. The variations in performance in the different simulation cases can be explained by the varying dataset size, where Case 5 has the lowest performance and a significantly smaller dataset size. As several FE simulations with varying geometries, deposition patterns, power intensities, and meshes was predicted with high performance, the results proves that the model is generic and can handle a wide range of simulation characteristics. This contrasts with the non-generic ML models previously proposed, and an important finding as realistic optimization requires ML models that may handle complex geometries and conditions.

The simulation-to-simulation predictions test several transferability scenarios and have, as expected, lower performance than the baseline tests. The reduced performance is expected as the ML models are trained on cases with different characteristics than what it is predicting. However, most investigations have MAPE below 10%, proving that the feature space captures significant parts of the thermal processes in AM. Still, the feature space needs to be refined and extended to capture all thermal processes in AM and thereby improve the ML performance. The findings nonetheless demonstrate the capability of simulation-to-simulation predictions of thermal fields in AM when both when the ML models are trained on one or multiple simulations.

In addition, the transferability of the models in terms of geometry, printing pattern, power energy and mesh has been compared to previous work in Table 10. It should be pointed out that most of the previous work did not perform simulation-to-simulation predictions to study the transferability of their models. The transferability of the previous models in different situations shown in Table 10 is evaluated by analyzing whether their input features can generally characterize the printing process or the models. As shown in the table, previous models only have transferability in certain aspects while our models can perform simulation-to-simulation predictions across different patterns, geometries, meshes, and power intensities. Moreover, the proposed model in this work requires less data than other models. In general,

compared with other models, the main advantage of this model is that it has transferability across different geometry, layers, patterns, and power density while requiring less training data.

7. Conclusions and future work

In this paper, predictions of nodal thermal histories in additive manufacturing have been performed by engineering a generic feature set. The features were designed based on the underlying physics of the thermal processes during manufacturing. The data were generated through various FE simulations with different part geometries, deposition patterns, meshes, and power intensities. Testing different cases proved that the generic feature set has high performance, both for same-simulation and simulation-to-simulation predictions. Our work proves that simulation-to-simulation predictions are possible with high accuracy (MAPE below 10%) across different patterns, geometries, meshes, and power intensities. This demonstrates the potential of data-driven modeling in AM and thus accelerates the adoption of AM as a commonly used manufacturing technology. Further, the thermal behavior of layers deposited in the future was predicted with a MAPE of 5.808%. These findings show promise to reduce the time and computational cost compared to traditional numerical methods and is a step towards real-time optimization in additive manufacturing.

In the future work, we plan on developing features that cover an even more comprehensive range of properties, such as different materials, printing bases, geometries. Although, predictions of several geometries and patterns have been performed, it is not yet exhaustive. The models are of demonstrative nature, and more realistic models must therefore be included in the future. Furthermore, we plan to develop a combinatorial database of simulations to train faster and more robust ML models, where data from hundreds of thousands of simulations could contain yet-undiscovered patterns and thermal relations in AM. Although the work presented in this paper is limited to AM, the method is possible to extend to other manufacturing processes where thermal fields are of interest.

8. Declaration of Competing Interest

The authors declare that they have no known competing financial interests or personal relationships that could have appeared to influence the work reported in this paper.

Appendix A. Simulation details

Details of the simulated AM models		
Material properties	Material	AA2319
Boundary conditions	Thermal	Constant base temp. of T_{am}
Geometrical properties	Base height (h_b)	0.02 m
Process parameters	Layer thickness	0.0023 m
	Pass width (a)	0.01 m
	T_{am}	20 °C
	Print speed (v)	0.015 m/s
Mesh details	Element size	0.005 m
	Element type	DC3D8
	Integration	Full
Deposition details	Activation offset	0.005 m
	Activation set size	$(0.005 \times 0.01 \times 0.0023)$ m^3
	Heat source model	Double ellipsoid
	a_f	0.002 m
	a_r	0.004 m
	f_f	0.6
	f_r	1.4
	Layer break	10 s

Appendix B. Feature partial dependence

As a last step in the feature engineering process, partial dependence plots were produced on the feature space. Partial dependence plots illustrate the marginal effects of the features on the target value of a ML model, and is used to get an understanding of the dependence of approximations done by the ML model. The partial dependence plots of the features can be seen in Fig. B.12, where the blue lines gives an indication of the ML model's prediction of the temperature based on the given feature.

All the features displayed has the expected and wanted response, as described when the features were introduced earlier in this section. As an example it can be seen in Fig. B.12 that the nodal temperature would be predicted to be high if the feature has a low numerical value, and that it would be predicted to be significantly lower if d_e had a high numerical value. Opposite to this *VR* would predict low temperatures for low numerical values of *VR* (corresponding to nodes close to free surfaces) and higher temperatures if *VR* has high numerical values.

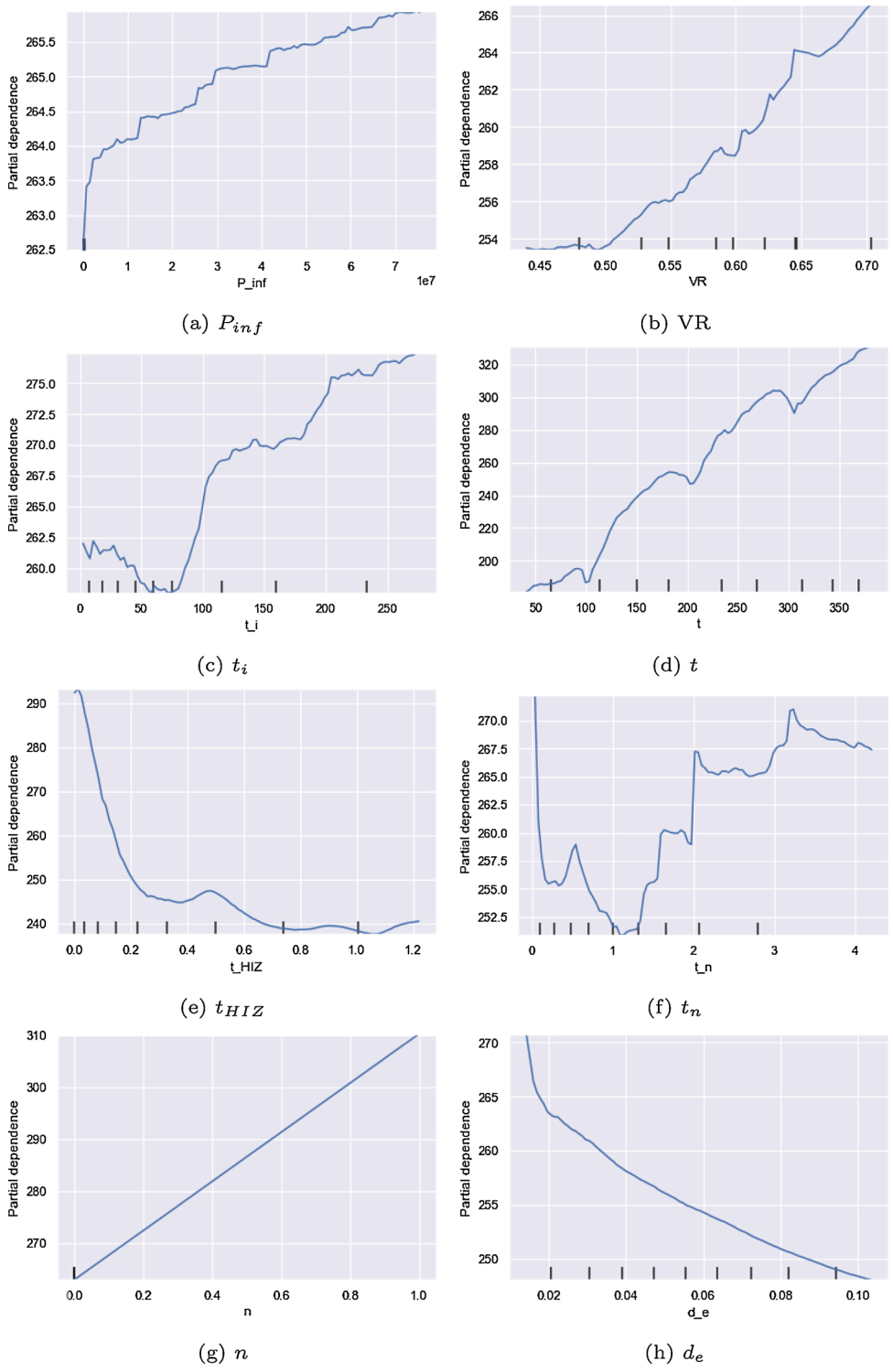

Fig. B.12. Partial dependence plots of feature space, where feature value is plotted with the partial dependence.

Appendix C. Material properties

C.1 Aluminium alloy 2319 (AA2319)

The material properties have been found in *Evaluation of 2D and 3D FEA Models for Predicting Residual Stress and Distortion* by Gouge and Michaleris (2017). The temperature dependent properties can be seen in Fig. C.13 and temperature-independent properties can be seen in Table C.11.

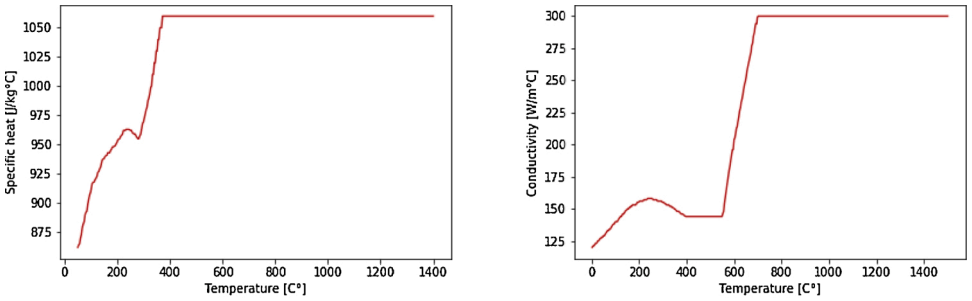

(a) Specific Heat (b) Conductivity

Fig. C.13. Temperature dependent properties for AA2319.

Table C.11
Temperature independent properties of AA2319.

AA2319	
Mass density	2823 kg/m^3
Liquidus temperature	643 °C
Solidus temperature	543 °C

References

Adinarayanappa, M., Kumar, S., Kumar, M.N., Chinthapenta, A., Simhambhatla, V.S., 2017. Investigations into effect of weld-deposition pattern on residual stress evolution for metallic additive manufacturing. Int. J. Adv. Manuf. Technol. 90.

Altmann, A., Toloşi, L., Sander, O., Lengauer, T., 2010. Permutation importance: a corrected feature importance measure. Bioinformatics 26 (10), 1340–1347.

Barber, C.B., Dobkin, D.P., Huhdanpaa, H., 1996. The quickhull algorithm for convex hulls. ACM Trans. Math. Softw. 22 (4), 469–483.

Berman, K.A., Paul, J.L., 2005. Algorithms: Sequential, Parallel, and Distributed. Course Technology Ptr.

Breiman, L., 2001. Random forests. Mach. Learn. 45 (1), 5–32.

Carslaw, H.S., Jaeger, J.C., 1959. Conduction of Heat in Solids, Technical Report. Clarendon Press.

Chew, Y., Pang, J.H.L., Bi, G., Song, B., 2015. Thermo-mechanical model for simulating laser cladding induced residual stresses with single and multiple clad beads. J. Mater. Process. Technol. 224, 89–101 https://www.sciencedirect.com/science/article/pii/S0924013615001971.

DebRoy, T., Wei, H., Zuback, J., Mukherjee, T., Elmer, J., Milewski, J., Beese, A.M., Wilson-Heid, A., De, A., Zhang, W., 2018. Additive manufacturing of metallic components-process, structure and properties. Prog. Mater. Sci. 92, 112–224.

Fetni, S., Pham, Q.D.T., Tran, V.X., Duchêne, L., Tran, H.S., Habraken, A.M., 2021. Thermal Field Prediction in DED Manufacturing Process Using Artificial Neural Network.

Géron, A., 2019. Hands-on Machine Learning with Scikit-Learn, Keras, and TensorFlow: Concepts, Tools, and Techniques to Build Intelligent Systems. O'Reilly Media.

Geurts, P., Ernst, D., Wehenkel, L., 2006. Extremely randomized trees. Mach. Learn. 63 (1), 3–42.

Gouge, M., Michaleris, P., 2017. Thermo-Mechanical Modeling of Additive Manufacturing. Elsevier Science & Technology.

Groover, M.P., 2016. Groover's Principles of Modern Manufacturing: Materials, Processes, and Systems. Wiley Global Education.

James, G., Witten, D., Hastie, T., Tibshirani, R., 2014. An introduction to statistical learning-with applications in R. Int. Stat. Rev. 82, 26.

Jiang, P., Zhou, Q., Shao, X., 2020. Surrogate Model-Based Engineering Design and Optimization. Springer.

Kourou, K., Exarchos, T.P., Exarchos, K.P., Karamouzis, M.V., Fotiadis, D.I., 2015. Machine learning applications in cancer prognosis and prediction. Comput. Struct. Biotechnol. J. 13, 8–17.

Lee Rodgers, J., Nicewander, W.A., 1988. Thirteen ways to look at the correlation coefficient. Am. Stat. 42 (1), 59–66.

Liashchynskyi, P., Liashchynskyi, P., 2019. Grid Search, Random Search, Genetic Algorithm: A Big Comparison for NAS arXiv preprint arXiv:1912.06059.

Mitchell, T.M., 1997. Machine Learning. McGraw-Hill Education.

Mozaffar, Mojtaba, Liao, Shuheng, Lin, Hui, Ehmann, Kornel, Cao, Jian, 2021. Geometry-agnostic data-driven thermal modeling of additive manufacturing processes using graph neural networks. Additive Manufacturing 48.

Mozaffar, M., Paul, A., Al-Bahrani, R., Wolff, S., Choudhary, A., Agrawal, A., Ehmann, K., Cao, J., 2018. Data-driven prediction of the high-dimensional thermal history in directed energy deposition processes via recurrent neural networks. Manuf. Lett. 18, 35–39.

Oliveira, J., Santos, T., Miranda, R., 2020. Revisiting fundamental welding concepts to improve additive manufacturing: from theory to practice. Prog. Mater. Sci. 107, 100590 https://www.sciencedirect.com/science/article/pii/S0079642519300726.

o'Rourke, J., 1998. Computational Geometry in C. Cambridge university press.

Ozdemir, S., Susarla, D., 2018. Feature Engineering Made Easy: Identify Unique Features from your Dataset in Order to Build Powerful Machine Learning Systems. Packt Publishing Ltd.

Paul, A., Mozaffar, M., Yang, Z., Liao, W.-k., Choudhary, A., Cao, J., Agrawal, A., 2019. A real-time iterative machine learning approach for temperature profile prediction in additive manufacturing processes. 2019 IEEE International Conference on Data Science and Advanced Analytics (DSAA), IEEE 541–550.

Pearson, K., 1896. Mathematical contributions to the theory of evolution. III. Regression, heredity, and panmixia. Philos. Trans. R. Soc. Lond. Ser. A 187, 253–318.

Pham, T.Q.D., Hoang, T.V., Pham, Q.T., Huynh, T.P., Tran, V.X., Fetni, S., Duchêne, L., Tran, H.S., Habraken, A.M., 2021. Data-Driven Prediction of Temperature Evolution in Metallic Additive Manufacturing Process.

Ren, K., Chew, Y., Zhang, Y., Fuh, J., Bi, G., 2020. Thermal field prediction for laser scanning paths in laser aided additive manufacturing by physics-based machine learning. Comput. Methods Appl. Mech. Eng. 362, 112734.

Roy, M., Wodo, O., 2020. Data-driven modeling of thermal history in additive manufacturing. Addit. Manuf. 32, 101017 https://www.sciencedirect.com/science/article/pii/S2214860419307249.

Roy, M., Wodo, O., 2021. Feature engineering for surrogate models of consolidation degree in additive manufacturing. Materials 14 (9), 2239.

Spearman, C., 1904. The proof and measurement of association between two things. Am. J. Psychol. 15 (1), 72–101 http://www.jstor.org/stable/1412159.

Stathatos, E., Vosniakos, G.-C., 2019. Real-time simulation for long paths in laser-based additive manufacturing: a machine learning approach. Int. J. Adv. Manuf. Technol. 104 (5), 1967–1984.

Sun, L., Ren, X., He, J., Olsen, J.S., Pallaspuro, S., Zhang, Z., 2019. A new method to estimate the residual stresses in additive manufacturing characterized by point heat source. Int. J. Adv. Manuf. Technol. 105 (5), 2415–2429.

Sun, L., Ren, X., He, J., Zhang, Z., 2021a. A bead sequence-driven deposition pattern evaluation criterion for lowering residual stresses in additive manufacturing. Addit. Manuf. 102424.

Sun, L., Ren, X., He, J., Zhang, Z., 2021b. Numerical investigation of a novel pattern for reducing residual stress in metal additive manufacturing. J. Mater. Sci. Technol. 67, 11–22 https://www.sciencedirect.com/science/article/pii/S1005030220306897.

Watson, J., Taminger, K., 2018. A decision-support model for selecting additive manufacturing versus subtractive manufacturing based on energy consumption. J. Clean. Prod. 176, 1316–1322 https://www.sciencedirect.com/science/article/pii/S0959652615018247.

Zhou, Z., Shen, H., Liu, B., Du, W., Jin, J., 2021. Thermal field prediction for welding paths in multi-layer gas metal arc welding-based additive manufacturing: a machine learning approach. J. Manuf. Process. 64, 960–971.